Characterization of concomitant gradient fields and their effects on image distortions using a low-field point-of-care Halbach-based MRI system

de Vos, Bart; Remis, Rob F.; Webb, Andrew G.

DOI
10.1002/mrm.29879

Publication date
2023

Document Version
Final published version

Published in
Magnetic Resonance in Medicine

Received: 15 May 2023 | Revised: 7 September 2023 | Accepted: 8 September 2023

DOI: 10.1002/mrm.29879

RESEARCH ARTICLE

Magnetic Resonance in Medicine

Characterization of concomitant gradient fields and their effects on image distortions using a low-field point-of-care Halbach-based MRI system

Bart de Vos[1] | **Rob F. Remis**[2] | **Andrew G. Webb**[1,3]

[1]Radiology, C.J. Gorter MRI Center, Leiden University Medical Center, Leiden, The Netherlands

[2]Micro-electronics, Signal Processing Systems, Delft University of Technology, Delft, The Netherlands

[3]Micro-electronics, Terahertz Sensing, Delft University of Technology, Delft, The Netherlands

Correspondence
Bart de Vos, Radiology, C.J. Gorter MRI Center, Leiden University Medical Center, LUMC Main Building, Albinusdreef 2, 2333 ZA, Room number: J0-56, Leiden, The Netherlands.
Email: b.de_vos@lumc.nl

Funding information
H2020 European Research Council, Grant/Award Number: 101021218

Abstract

Purpose: Concomitant gradient fields have been extensively studied at clinical field strengths. However, their effects have not yet been modeled for low-field point-of-care (POC) systems. The purpose of this work is to characterize the effects associated with concomitant fields for POC Halbach-array-based systems.

Methods: The concomitant fields associated with a cylindrical gradient coils designed for a transverse B_0 and a signal model including the tilting effect of the effective magnetic field are derived. The formalism is used to simulate and predict concomitant field related distortions. A 46-mT Halbach-array-based system with a maximum gradient strength of 15 mT/m is used to verify the model using two-dimensional spin-echo sequences.

Results: The simulations and experimental results are in good agreement with the derived equations. The fundamental characteristics of the concomitant field equations are different to conventional MRI systems: Image distortions occur primarily in the transverse directions and a cross-term only exists when applying transverse gradient pulses simultaneously.

Conclusion: The level of image warping in the frequency encoding direction is insignificant for the POC systems discussed here. However, when trying to achieve short echo-times by using strong phase encoding and readout-dephasing gradients, the combination can result in image warping and blurring which should be accounted for in image interpretation.

KEYWORDS
concomitant fields, Halbach-array, image distortions, low-field

1 | INTRODUCTION

Recently, there has been significant interest in low-field point-of-care (POC) MRI systems[1-4] which can be used in environments where MRI is currently lacking: examples include the intensive care unit,[5,6] the emergency room, and regions in low- and middle-income countries with limited financial and infrastructural resources.[7,8] These low-field systems typically have magnetic fields between approximately 40 and 80 mT, run on mains power and do not use cooling. The gradient field strengths are lower compared to conventional clinical systems

and are typically on the order of 10–20 mT/m. These magnetic field gradients have undesired but unavoidable vector-components known as concomitant fields, since the magnetic flux density must be divergence- and curl-free in a source-free region under quasi-static conditions. These components change the desired magnitude and direction of the magnetic flux density, potentially creating pulse sequence-dependent image artifacts.[9] The severity of concomitant field effects can be characterized by a dimensionless quantity ϵ:[10-12]

$$\epsilon = \frac{G_{\max} L}{B_0}, \quad (1)$$

where $G_{\max}$ is the maximum gradient strength, and L is the Field-of-View (FOV) in the direction of the gradient. This dimensionless quantity is useful when analyzing the effects of concomitant fields for different systems. For example, since POC systems typically operate at B_0 values 30 times lower than 1.5 T, and have maximum gradient strengths between three and five times less, the expectation is that concomitant gradient fields effects are much more significant.

Artifacts created by concomitant fields, and artifact reduction strategies, have been extensively studied at clinical field strengths. Bernstein et al.[13] gave an in-depth analysis of concomitant field effects in phase contrast angiography and first introduced the concept of concomitant field cross-terms, that is, the additional effects occurring when two or more gradients are applied simultaneously. Using a Taylor series, they derived a general expression for the magnitude of the magnetic flux density, in which the desired phase is separated from the undesired concomitant phase, a representation which is extensively used. They demonstrated that concomitant fields create shading artifacts in phase contrast MRI, using a FOV of 320 mm, $B_0 = 1$ T and $G_{\max} = 22$ mT/m ($\epsilon = 0.007$). To mitigate these effects, modifications to the pulse sequence were proposed, which were effective but led to increased echo and/or repetition time. They also demonstrated a reconstruction method to predict the concomitant field phase errors and correct for them during postprocessing. Concomitant field effects have also been studied for nonaxial[14] and axial echo planar imaging (EPI).[15] In axial EPI, concomitant fields created a displacement of the object in the phase encoding direction, the magnitude of which is quadratically dependent on the axial position. The shift was visible in a slice 40 mm from iso-center using a field strength of 1.5 T, an FOV of 260 mm and a readout gradient strength of 21.6 mT/m, ($\epsilon = 0.0037$).[15] Image ghosting was also observed for larger values of ϵ. To remove the parabolic shift, the receiver phase was adjusted; another technique used compensation gradients to remove the phase error. For nonaxial EPI a pixel-by-pixel correction algorithm was demonstrated which corrects for the phase errors before reconstruction.[16] King et al.[17] demonstrated that concomitant fields can create blurring when using spiral trajectories with the following system parameters: $B_0 = 1.5$ T, FOV = 200 mm and $G_{\max} = 21$ mT/m ($\epsilon = 0.0028$). In-plane blurring corrections were performed by adapting an algorithm used for chemical shift and susceptibility offsets.[18,19] Through-plane blurring was corrected by dynamically shifting the receive frequency. Zhou et al.[20] demonstrated that fast spin echo sequences with large FOV's can result in ghosting artifacts. These artifacts were visible imaging the spinal cord using a FOV of 480 mm, $B_0 = 1.5$ T, $G_{max} = 22$ mT/m ($\epsilon = 0.007$). They mitigated these effects by adding compensation pulses.

Early work regarding concomitant fields at low-field was performed by Norris and Hutchison[21] who used a parallel plate, open, resistive magnet with a field strength of 0.04 T and a single quadrupolar gradient coil. These cylindrical coils are also used for Halbach-based systems as they create a quadrupolar field, where the transverse component can be used as a z-gradient when considering a transverse B_0 field. A bipolar gradient pulse was added to a spin echo pulse sequence to create additional concomitant phase, and it was demonstrated that this phase agrees with the theory by imaging a disk phantom. Volegov et al.,[22] created a signal model for a gradient echo pulse sequence at very low-field strengths ($B_0 = 0.0001$T, FOV = 300 mm and $G_{\max} = 0.05$ mT/m ($\epsilon = 0.15$)) not only taking into account the errors created by the phase differences but also the errors created by the tilting of the effective magnetic field. In simulations they demonstrated that the phase differences caused blurring in the phase encoding direction, and displacement in the readout direction. The tilt was shown to cause additional blurring, shading, and a ghosting artifact. Clarke et al.[12] used a low-field system which used prepolarization and superconducting quantum interference devices combined with $B_0 = 66$ μT, $G_{\max} = 350$ μ T/m and a FOV of 175 mm ($\epsilon = 0.15$). Using spin-echo images they showed distortions in a grid phantom. They proposed a dewarping and phase correction model, not including the tilting effect. A more general approach was taken by Yablonskiy et al.,[11] who studied the possible geometric distortions different gradients, such as slice select, phase encoding and readout can create due to concomitant fields. More recently, Wang et al.[23] demonstrated a compensation scheme for dealing with concomitant gradient field effects in two-dimensional (2D) spiral TSE at 0.55 T using compensation pulses to eliminate the undesired phase and comparing their results with a 1.5 T system.

The spatial distribution of concomitant fields depend on the gradient coil geometry, influencing where the artifacts occur, which gradients can be used simultaneously

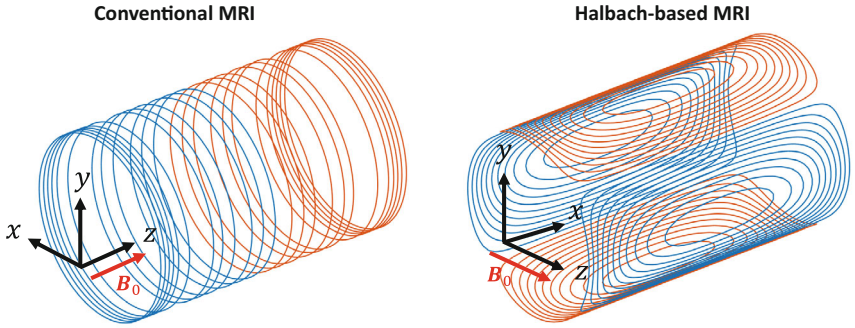

FIGURE 1 Left: illustration of a typical wire pattern for a z-gradient coil used in conventional MRI systems. Right: illustration of a typical z-gradient coil used in Halbach-based MRI systems. Corresponding coordinate systems are displayed with each gradient coil.

without introducing a cross-term, and the artifact correction scheme. Previous literature, surveyed above, concentrates on cylindrical systems with the B_0 parallel to axis of the magnet bore or systems with a transverse B_0 combined with bi-planar gradient coils.[9] However, the equations defining the concomitant fields do not hold for cylindrical gradient coils designed for a transverse B_0 field, which is the case for Halbach-array-based magnets.[24-28]

In this work the concomitant fields associated with Halbach-based MRI systems are characterized. Furthermore, the distortions that these fields can potentially create in low-field POC systems are analyzed and compared to conventional systems. A general signal model is derived which can be used to simulate the effects of concomitant fields and includes the tilting effects. This model is verified using spin-echo sequence on a 46-mT Halbach-based system, with a maximum gradient strength of 15 mT/m and a FOV of 250 mm ($\epsilon = 0.082$).

2 | THEORY

The case is considered where three linear gradient fields are used for spatial encoding and B_0 is directed along the z-direction. The z-component of the magnetic flux density can then be expressed as

$$B_z = B_0 + G_x x + G_y y + G_z z = B_0 + \mathbf{g}^T \mathbf{r}, \tag{2}$$

where $\mathbf{g} = [G_x, G_y, G_z]^T$ and $\mathbf{r} = [x, y, z]^T$. Under quasi-static conditions, Maxwell's equations require that in a source-free region, the magnetic flux density must be curl- and divergence-free. Given these requirements and Equation (2), the components of the magnetic flux density can be written in the form[9]

$$\begin{bmatrix} B_x \\ B_y \\ B_z - B_0 \end{bmatrix} = \begin{bmatrix} -\alpha G_z & G_\perp & G_x \\ G_\perp & (\alpha - 1) G_z & G_y \\ G_x & G_y & G_z \end{bmatrix} \begin{bmatrix} x \\ y \\ z \end{bmatrix}, \tag{3}$$

where $G_\perp$ is the transverse gradient term which is zero for both conventional MRI and Halbach-based systems. The divergence-free requirement allows multiple solutions regarding the concomitant fields associated with the z-gradient, which is captured by the variable α and is specified by the gradient coil geometry. In conventional MRI the B_0 field is directed along the axis of the bore. Figure 1 illustrates the associated Helmholtz type (fingerprint) coil, which creates an equal distribution of the concomitant components in the x- and y-direction, resulting in $\alpha = 1/2$. This value also holds for parallel plate gradient coils in an open C- or H-shaped magnet.[9] In contrast, a Halbach-array-based magnet creates a B_0 field directed transverse to the bore. The corresponding z-gradient has a quadrupolar geometry[29] and the magnetic flux density associated with these coils has no x-component in the linear region of interest (along the bore), leading to $\alpha = 0$.

Having determined the gradient field structure for Halbach-systems, the magnitude of the magnetic flux density can be described using a Taylor series

$$|\mathbf{B}| \approx B_0 + \mathbf{g}^T \mathbf{r} + \frac{1}{2B_0}\left[(G_x^2 + G_y^2) z^2 + G_z^2 y^2 - 2 G_y G_z yz\right] + \frac{1}{2B_0^2}(\dots), \tag{4}$$

where for sufficiently large values of B_0 only the $\frac{1}{2B_0}$ terms of the expansion are taken into account. The general form (including α and $G_\perp$) up to third order can be found in Reference 13. A shorter form of the above equation where the desired part is separated from the concomitant fields is

$$|\mathbf{B}(\mathbf{g})| \approx B_0 + \mathbf{g}^T \mathbf{r} + g^c(\mathbf{g}), \tag{5}$$

where, in this notation, it is explicitly indicated that $|\mathbf{B}|$ depends on the gradient vector g, and g^c describes the contribution due to the concomitant fields. As mentioned above, it is often sufficient to take

$$g^c(\mathbf{g}) \approx \frac{1}{2B_0}\left[(G_x^2 + G_y^2) z^2 + G_z^2 y^2 - 2 G_y G_z yz\right] = \frac{1}{2B_0}\left[(G_y z - G_z y)^2 + G_x^2 z^2\right] \geq 0, \tag{6}$$

as long as B_0 is sufficiently large. In the first line of expression three self-squared and a single cross-term can be distinguished, where the cross-term only exists when G_y and G_z are applied simultaneously. The first term in Equation (6) is also present in the conventional[9] concomitant field expression. However, the main difference is that the quadrupolar field created by the z-gradient of a Halbach-based system has a single concomitant component in the region of interest ($\alpha = 0$), and is therefore significantly different to its conventional counterpart ($\alpha = 1/2$). This is why Halbach-based systems using a quadrupolar z-gradient only have a single cross-term with twice the strength which is independent of the spatial coordinate x. The concomitant fields described here are therefore independent of the conventional expression. Comparing the above equation to the concomitant fields associated with conventional MRI,[13] three distinct differences can be observed:

1. There is only a single cross-term which is present when simultaneously applying the transverse y and z gradients. In conventional MRI, combining z and x also results in a cross-term.
2. The cross-term has double the amplitude of a conventional MRI cross-term.
3. whereas the concomitant fields increase with the axial position for the conventional case, concomitant field effects increase in the transverse directions for Halbach-based MRI. There is no axial dependency in the main term of this expansion, meaning there is little to no dependency on the longitudinal x coordinate.

2.1 | Signal model

A general signal model is derived to simulate the artifacts created by concomitant fields. The solution of the Bloch equations, not taking into account relaxation times, can be written as (see Appendix)

$$\mathsf{m}(\mathsf{g}, t) = \rho(\mathsf{r}')\mathsf{X}e^{-\mathrm{j}\gamma|\mathbf{B}(\mathsf{g})|\mathsf{S}t}\mathsf{X}^H\tilde{\mathsf{m}}_0, \tag{7}$$

where $\mathsf{m}(\mathsf{g}, t) = [M_x, M_y, M_z]^T$ contains the components of the magnetization and the initial magnetization is specified with $\tilde{\mathsf{m}}_0 = \left[M_x^0, M_y^0, M_z^0\right]^T$, where the spin density $\rho(\mathsf{r}')$ is factored out. Furthermore, $\mathsf{X} = \mathsf{X}(\mathsf{g})$ is a unitary matrix with the eigenvectors of the Bloch system matrix (specified in the appendix) as its columns. Furthermore, superscript H denotes the hermitian transpose, S is a diagonal matrix given by $\mathsf{S} = \mathrm{diag}(-1, 0, 1)$, and j is the imaginary unit.

Subsequently, two gradient vectors are introduced. Specifically, $\mathsf{g}^{\mathrm{pe}} = [G_x^{\mathrm{pe}}, G_y^{\mathrm{pe}}, G_z^{\mathrm{pe}}]^T$ is the gradient vector characterizing the gradients used during phase encoding and $\mathsf{g}^{\mathrm{r}} = [G_x^{\mathrm{r}}, G_y^{\mathrm{r}}, G_z^{\mathrm{r}}]^T$ the gradient vector during frequency encoded data-acquisition. Assuming that the phase encoding gradients are applied for τ seconds, the resulting magnetization is given by

$$\mathsf{m}_{\mathrm{pe}} := \mathsf{m}(\mathsf{g}^{\mathrm{pe}}, \tau) = \rho(\mathsf{r}')\ \mathsf{P}\ e^{-\mathrm{j}\gamma|\mathbf{B}(\mathsf{g}^{\mathrm{pe}})|\mathsf{S}\tau}\ \mathsf{P}^H\tilde{\mathsf{m}}_0, \tag{8}$$

with $\mathsf{P} = \mathsf{X}(\mathsf{g}^{\mathrm{pe}})$. Furthermore, after the phase encoding step, the magnetization during data-sampling can be written as

$$\mathsf{m}_{\mathrm{r}}(t) := \mathsf{m}(\mathsf{g}^{\mathrm{r}}, t) = \mathsf{Q}e^{-\mathrm{j}\gamma|\mathbf{B}(\mathsf{g}^{\mathrm{r}})|\mathsf{S}t}\ \mathsf{Q}^H\mathsf{m}_{\mathrm{pe}}, \tag{9}$$

with $\mathsf{Q} = \mathsf{X}(\mathsf{g}^{\mathrm{r}})$. Note that in most imaging sequences m_{r} remains constant between phase encoding steps, with only m_{pe} changing. The voltage induced in the coil during data sampling is given by[30]

$$v(t) = -\int_{\mathbf{r}'\in V} \mathsf{b}^H \frac{\partial \mathsf{m}_{\mathrm{r}}(t)}{\partial t}\, \mathrm{d}V, \tag{10}$$

where $\mathsf{b} = [\beta_x, \beta_y, \beta_z]^T$ is the coil sensitivity. Subsequently, this signal is demodulated with modulation frequency $\omega_0 = \gamma B_0$ and low pass filtered to obtain the signal

$$s(t) = \mathrm{lowpass}\left\{v(t)e^{-\mathrm{j}\omega_0 t}\right\}. \tag{11}$$

Using the above expression for $\mathsf{m}_{\mathrm{r}}(t)$ this signal is given by

$$s(t) = -\mathrm{j}\int_{\mathbf{r}'\in V} \gamma|\mathbf{B}(\mathsf{g}^{\mathrm{r}})|\ (\mathsf{b}^H\mathsf{q}_{-1})\ (\mathsf{q}_{-1}^H\mathsf{m}_{\mathrm{pe}})\ e^{\mathrm{j}[\gamma|\mathbf{B}(\mathsf{g}^{\mathrm{r}})|-\omega_0]t}\, \mathrm{d}V. \tag{12}$$

Finally, substituting Equation (8) in the above expression results in

$$s(t) = -\mathrm{j}\sum_{\ell=-1}^{+1}\int_{\mathbf{r}'\in V} \rho(\mathsf{r}')\ \gamma|\mathbf{B}(\mathsf{g}^{\mathrm{r}})|w_\ell\ e^{\mathrm{j}\varphi_\ell(t)}\, \mathrm{d}V, \tag{13}$$

with phases given by

$$\varphi_\ell(t) = [\gamma|\mathbf{B}(\mathsf{g}^{\mathrm{r}})| - \omega_0]t - \gamma|\mathbf{B}(\mathsf{g}^{\mathrm{pe}})|\tau\ \ell, \tag{14}$$

and weights

$$w_\ell = (\mathbf{b}^H\mathbf{q}_{-1})(\mathbf{q}_{-1}^H\mathbf{p}_\ell)(\mathbf{p}_\ell^H\tilde{\mathbf{m}}_0), \tag{15}$$

for $\ell = -1, 0, 1$, similar to Volegov.[22] The weighting can be split up in three parts: $(\mathbf{b}^H\mathbf{q}_{-1})$ describes the relationship between the readout frequency encoding gradient and the receive sensitivity of the coil, while the term $(\mathbf{q}_{-1}^H\mathbf{p}_\ell)$ describes the interaction between phase encoding and readout field. Finally, $(\mathbf{p}_\ell^H\tilde{\mathbf{m}}_0)$ represents the interaction between the phase encoding field and the initial magnetisation. If concomitant fields effects in the weighting

are not considered, only mode $\ell = -1$ remains, leaving only the concomitant field phase errors in the exponential, simplifying the model significantly.

2.1.1 | Simplified model including phase errors only

If concomitant field effects in the weighting are not considered, that is, the tilting effect is ignored, the elements of the Bloch matrix U shown in Appendix are $u_x = u_y = 0$ and $u_z = 1$, leading to P = Q and

$$w_{-1} = \mathsf{b}^H \mathsf{q}_{-1} \mathsf{q}_{-1}^H \tilde{\mathsf{m}}_0, \qquad w_0 = w_{+1} = 0.$$

Furthermore, $\mathsf{q}_{-1} = (1/\sqrt{2})[\mathrm{j}, -1, 0]^T$ and consequently

$$w_{-1} = \beta^+ \tilde{M}_0^-, \tag{16}$$

where $\beta^+ = \beta_x + \mathrm{j}\beta_y$ and $\tilde{M}_0^- = \tilde{M}_x^0 - \mathrm{j}\tilde{M}_y^0$. The other simplification to be made is that concomitant field effects in $\gamma|\mathbf{B}(\mathsf{g}^{\mathrm{r}})|$ only play a part in the phase. This leads to the final equation for the simplified model

$$s(\mathsf{k}) = -\mathrm{j} \int_{\mathbf{r}' \in V} \rho(\mathsf{r}')\ \omega_0 \beta^+ \tilde{M}_0^- e^{\mathrm{j}\ [\mathsf{k}^T \mathsf{r}' + \varphi^c(t) + \varphi_0]}\ \mathrm{d}V, \tag{17}$$

where $\mathsf{k} = \gamma(\mathsf{g}^r t + \mathsf{g}^{pe}\tau)$, the concomitant phase $\varphi^c(t) = \gamma\left[g^c(\mathsf{g}^{\mathrm{r}})t + g^c(\mathsf{g}^{\mathrm{pe}})\tau\right]$ and the phase offset $\varphi_0 = \gamma B_0 \tau$. If all concomitant field effects are ignored $\varphi^c(t) = 0$ and the conventional signal model remains. Simply taking the inverse Fourier transform of the above expression results in the effective spin-density $s(\mathsf{r})$, which can be written as the original spin density convolved with a point spread function (PSF)

$$s(\mathsf{r}) = \int_{\mathbf{r}' \in V} \rho(\mathsf{r}')\ P(\mathsf{r} - \mathsf{r}')\mathrm{d}V, \tag{18}$$

where

$$P(\mathsf{r} - \mathsf{r}') = -\frac{\mathrm{j}}{(2\pi)^3} \int_{\mathbf{k} \in \mathbb{R}^3} \omega_0 \beta^+ \tilde{M}_0^- e^{-\mathrm{j}\ [\mathsf{k}^T(\mathsf{r}-\mathsf{r}') - \varphi^c(t) - \varphi_0]}\ \mathrm{d}\mathbf{k}. \tag{19}$$

2.2 | Image artifacts

In this work spin-echo sequences are used as an example to characterize concomitant field effects. The frequency encoding gradient creates a phase error which is constant for each phase encoding line, but is spatially and gradient dependent. The undesired phase translates to a distorted spatial position. Taking a z-gradient as an example this can be shown by considering the resonance frequency with no distortions:

$$\omega(\mathbf{r}) = \gamma(\mathrm{B}_0 + G_z z), \tag{20}$$

and substituting Equations (5) and (6). This can then be rewritten to obtain

$$z_c = z + \frac{G_z y^2}{2B_0}. \tag{21}$$

where z_c is the distorted position, and z the intended location. This equation describes a parabolic shift in the direction of the readout gradient with the direction dependent on the polarity of the gradient.

In phase encoding the different amplitudes corresponding to each step translate to a summation of phase errors which leads to spatially and gradient dependent blurring. The position of this blurring can also be determined using Equation (6).

Gradients applied simultaneously can create a cross-term, with the associated distortions depending on the particular combination of gradients. If a constant gradient such as a dephasing frequency encoding gradient is simultaneous with the phase encoding gradient this creates blurring, as well as a warping effect. This warping effect for a z-gradient dephasing gradient, combined with a y-phase encoding gradient leads to

$$\Delta y = -\frac{G_z y z}{\mathrm{B}_0}. \tag{22}$$

Note the factor-of-two difference compared to the parabolic readout warp and the dependency on the sign of the y and z spatial coordinates. Therefore, the effect of the cross-term warping is more evident than the readout warping and also differs spatially.

The weighting w_ℓ creates multiplicative errors and is responsible for the distribution of the modes $\ell = -1, 0, +1$. The mode $\ell = +1$ create a phase opposing that of the dominant mode $\ell = -1$ mode, which can create a mirrored ghosting artifact. The mode $\ell = 0$ only creates a multiplicative error.

3 | METHODS

To verify the model and demonstrate the potential effects concomitant fields have on spin-echo images, a 46 mT Halbach-based system is used, similar to Reference 24. The system has a maximum gradient strength of 15 mT/m. At low B_0 fields, readout bandwidths rarely exceed 50 kHz (~4.5 mT/m using a 250 mm FOV), as high bandwidths degrade the signal-to-noise ratio. Therefore, concomitant effects will predominantly occur for the phase encoding

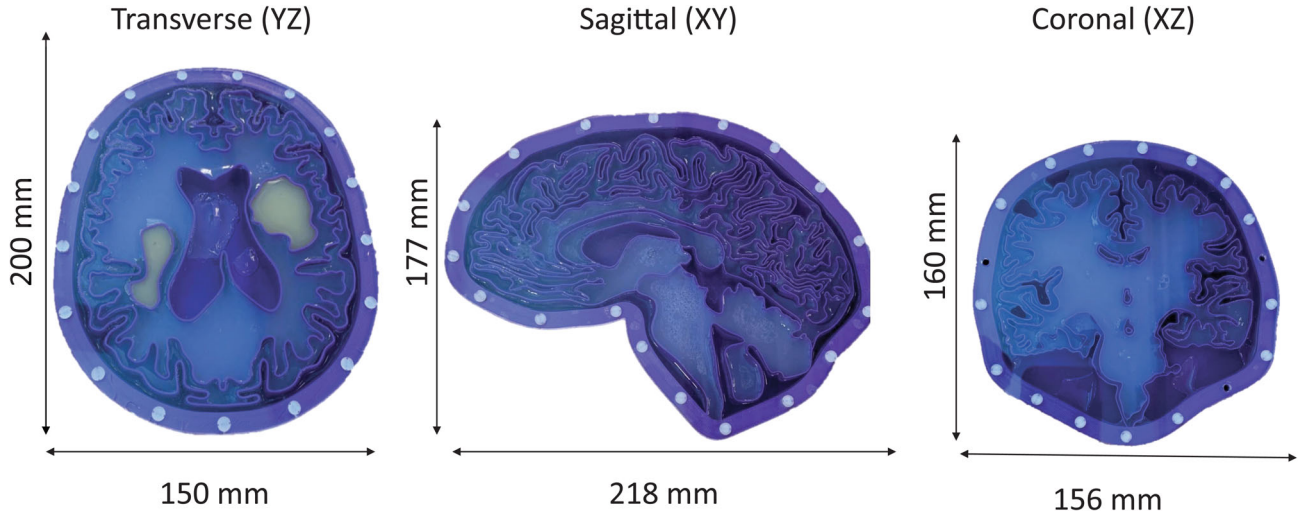

FIGURE 2 Two-dimensional brain phantoms corresponding to transverse, sagittal and coronal brain slabs. With relaxation parameters of the compartments approximately equal to in vivo data at 50 mT.[31] The dimensions are indicated in the figure and the thickness of the slabs are 20 mm. The phantoms where fabricated in-house using a three-dimensional printer and modeled using CAD software and 3T brain images.

and frequency encoding dephasing gradients which have high values to achieve short echo-times.

To verify Equation (6), specific for Halbach-array-based gradient coils, and show the effect of different encoding directions, 2D spin-echo images of the brain phantoms shown in Figure 2 were acquired and represent transverse, sagittal, and coronal slabs of the brain. As shown later, using the maximum gradient strength of 15 mT/m leads to very subtle distortions difficult to depict. To experimentally simulate the effects of higher gradient strengths a bipolar pulse was added as was done in Reference 21. This creates concomitant phase due to the quadratic dependency shown in Equation (6). The length of the bipolar pulse was determined to produce effects equivalent to those from a unipolar gradient field strength of 25 mT/m. The spin-echo sequences shown in Figure 3 were used, (A) shows the reference sequence, (B) the high gradient strength version including simultaneous gradients to demonstrate the cross-term effect, (C) the reference sequence with the addition of a bipolar phase encoding pulse and (D) the same sequence but with simultaneous phase and frequency dephasing gradients. The sequences were run for the three orthogonal planes on the corresponding brain phantoms. For each plane a reference image was acquired using the sequence of Figure 3A and a maximum gradient strength of 3.3 mT/m. These are compared to images obtained using Figure 3C,D with a simulated gradient strength of 25 mT/m. This was done twice for each plane to illustrate the effect on the distortions when switching the frequency and phase encoding axis. This leads to 2×12 images.

To verify that adding the bipolar pulse results in similar effects and to quantify the amount of warping, 2D spin-echo images of a tube phantom were acquired. The tube phantom consists of 37 tubes all with a diameter of 15 mm, separated 28 mm from each other and filled with doped water. To visualize the warping effect, images in the transverse yz-plane were acquired, since cross-term warping is expected to be observable in this plane. To show the effects, sequence (B) was used with the maximum possible gradient strength of 15 mT/m, and compared to the reference (using sequence (A) and 4 mT/m gradients). In addition, sequence (D) was used to simulate the gradient strength of 15 mT/m. The phantom was also simulated to verify the model. The simplified model shown in Equation (17) was used. The drawing of the phantom holder was used to create a binary mask for the spin density $\rho(\mathbf{r}')$, each k-space line, including the concomitant field phases was created with the scan parameters used for the measurements. Taking the inverse Fourier transform of the simulated k-space results in the spin density including concomitant field distortions.

Another way of visualizing the concomitant field error is to look at the effects on the phase of the signal. A measurement was performed following a similar approach as Bernstein et al.[13] A bottle with a diameter of 110 mm, filled with $CuSO_4$ doped water, was used as the phantom. As there is no flow in the phantom, a phase difference measurement using anti-symmetric bipolar pulses should not result in any phase variation throughout the phantom. However, concomitant field effects can create a residual phase. The self-squared terms cancel out, but the

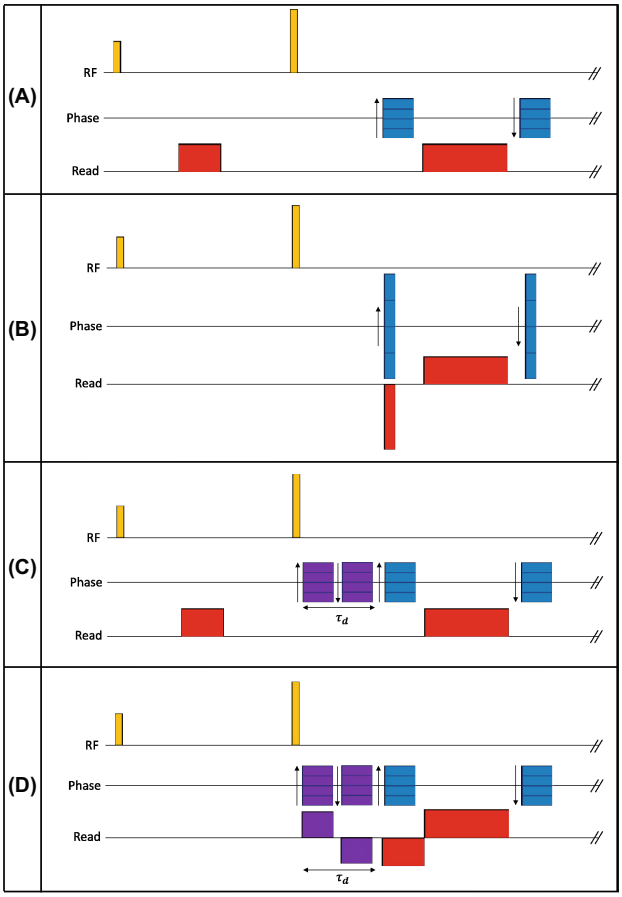

FIGURE 3 Sequence diagrams of the two-dimensional spin-echo sequences used to separately study the effects of the self-squared and cross-term from Equation (6). Red corresponds to the frequency encoding, blue the phase encoding and purple the additional bipolar pulses used to simulate the concomitant field phase effects of higher gradient strengths. (A) is used for the reference images, both the phase encoding and readout gradient use a maximum gradient strength of 4 mT/m. (B) is used to demonstrate the maximum concomitant field effects associated with this system, 15 mT/m gradients are used for the read-dephasing and maximum phase encoding strength. The read-dephasing and phase encoding are performed simultaneously. Pulse-squence (C) is the same as (A) but a bipolar pulse is added to simulate the concomitant field effects of stronger phase encoding gradient strengths. Finally, (D) is equivalent to (C) but now the dephasing is simultaneous with the phase encoding and the additional bipolar pulses are added to increase the cross-term effects.

cross-terms do not. Measurements were performed with gradient lobes applied sequentially and simultaneously to show this effect.

4 | RESULTS

Figure 4 shows images of the tube phantom in the yz-plane. The y-gradient (down-up) used for frequency encoding and the z-gradient (left-right) for the phase encoding, The one-dimensional profiles obtained from the tubes, shown at the bottom of the figure, confirm that the displacement created with sequence (B) and (D) is identical with respect to the reference figure (A). The maximum difference with respect to the reference tube is 1.4 mm. Considering Equation (22), a field strength of 46 mT, a gradient strength of 15 mT/m and the tubes being at spatial position: $y = 83$ and $z = 56$ mm, a 1.5 mm maximum displacement is expected. Considering the blurring which makes the border of the tube difficult to measure, this result is within expectations. The simulated experiments are created with the simplified model (Equation 17) and are in close correspondence with the measured profiles. This indicates that the effect of the modes $\ell = +1$ and $\ell = 0$ can be disregarded for this measurement setup as will be further shown in the discussion. note that the off-resonance effects created by inhomogeneities in the B_1^+ and B_0 fields create a visible difference in signal-to-noise ratio at the outer regions of the tube phantom. These differences are however constant between experiments and are therefore not associated with concomitant field effects.

Figure 5 shows the images resulting from the sequence of Figure 3A,C. Each row shows a different orientation in which a reference image using a maximum value of 3.3 mT/m for the phase encoding gradients is compared to a simulated gradient strength of 25 mT/m. Using Equation (6), blurring can be predicted and is indicated by the red arrow, while the green arrows indicate where no blurring should occur. The concomitant fields are expected to be constant in the x-direction, this is visible from the absence of distortions in the xy-plane (second row). The first row shows that changing the phase encoding gradient from z to y changes the blurring location in the phantom. The third row confirms that blurring only occurs when using the x-gradient for phase encoding in the zx-plane. The regions where blurring occurs are enlarged and compared to the reference scan. The figure shows that blurring gets worse for larger FOV's, this is most clear in the transverse plane (yz) where the top of the phantom shows significantly more blurring when compared to the sides of the phantom. The PSF in Equation (19) can be evaluated to quantify the amount of blurring. Using the scan parameters, the PSF at the edge of the phantom can be compared to the PSF at the center of the phantom. The result is shown in the Figure S1. It can be observed that the PSF at $y = 90$ mm is broadened by 2 mm.

The effect of simultaneous read-dephasing and phase encoding is shown in Figure 6, where the first row shows that simultaneously using the y- and z-gradients adds a warping effect with respect to the reference image, confirming the single cross-term. A difference image of

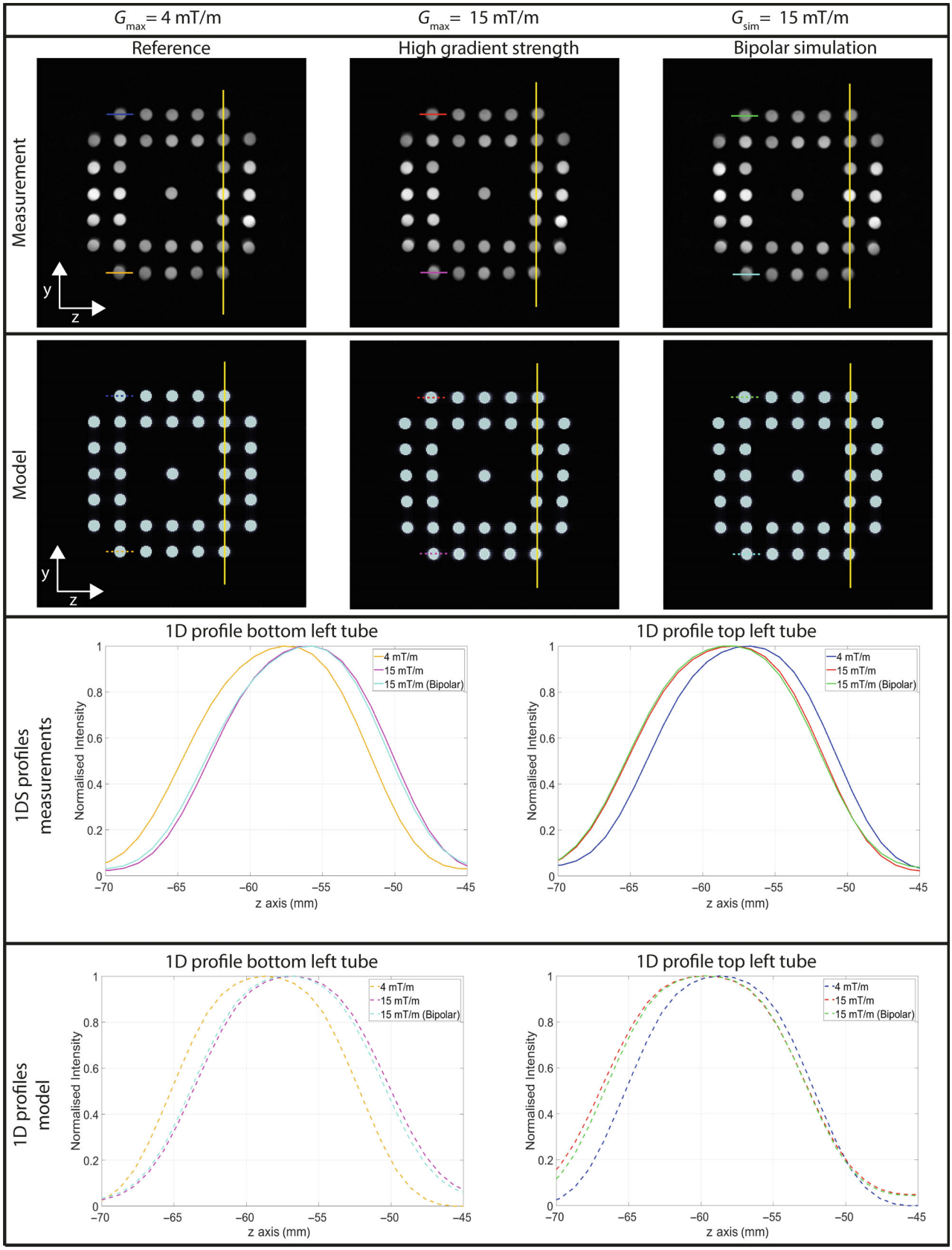

FIGURE 4 Comparison of tube phantom images with simulated data. The *yz*-plane is shown using the sequences of Figure 3 (A,B,D). Readout direction: y (down-up), phase encoding: z (left-right). A 1D profile through the top and bottom left tube demonstrates the blurring and displacement with respect to the simulation. The vertical yellow line is placed to help observe the warping effect. Acq param: FOV: 300x300 mm, Data Matrix: 300x300, TR/TE = 300/45 ms, BW = 50 kHz, τ_d = 11 ms, NA = 4.

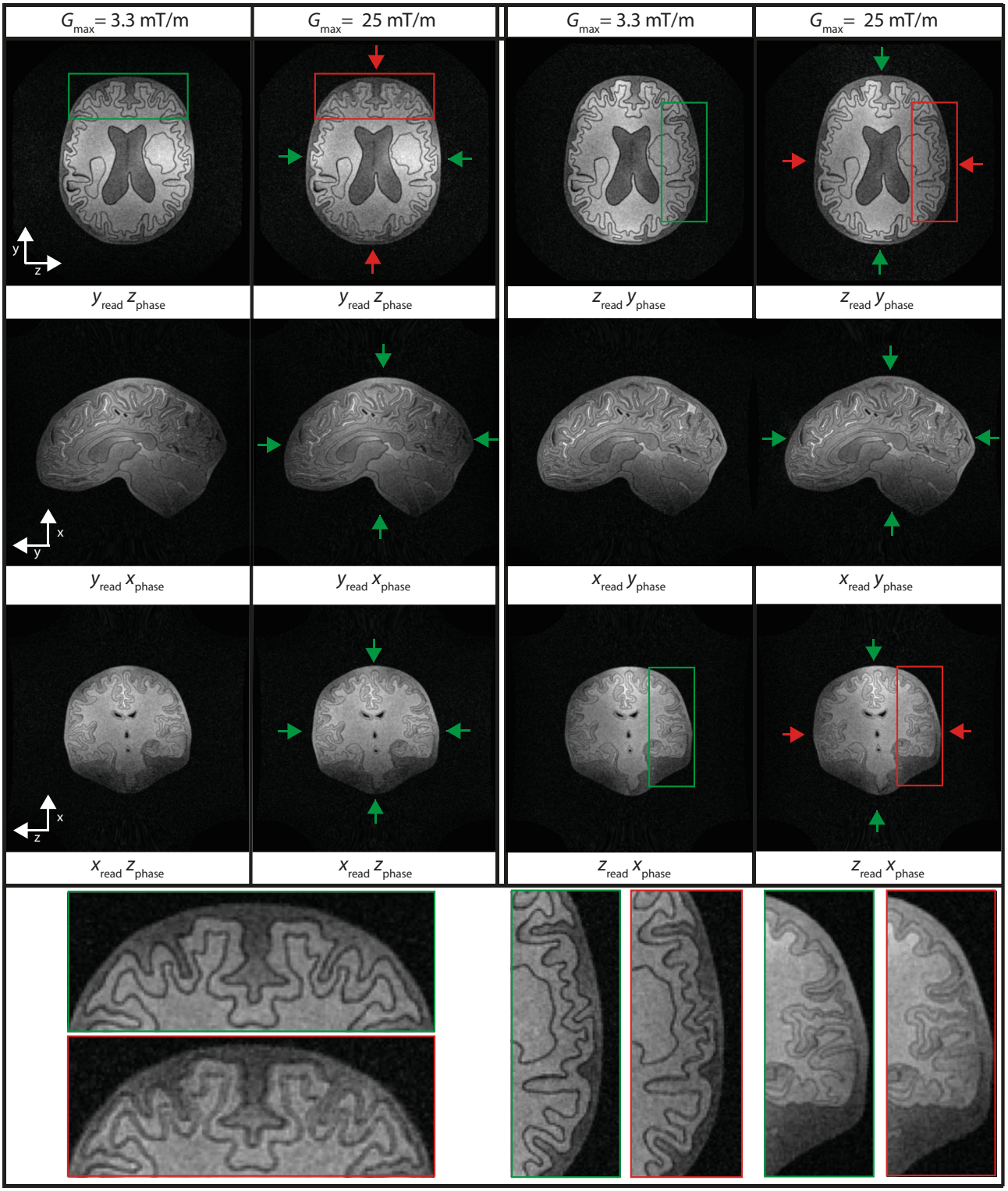

FIGURE 5 Phantom images obtained with the two-dimensional SE sequence shown in 3(A,C), used to show the self-squared term effects. Blurring is visible in certain orientations at the outer regions of the phantoms. red arrows show where blurring is expected, green where no distortions should occur according to Equation 6. Acq param: FOV: 280x280 mm, Data Matrix: 280x280, TR/TE = 900/65 ms, BW = 40 KHz, τ_d = 21 ms, NA = 6.

the reference and strong gradient image is shown at the bottom of the figure. The location of the warping rotates 90-degrees when interchanging frequency and phase encoding axis as is to be expected. From the other rows it becomes clear that the other gradients can be used simultaneously without additional effects.

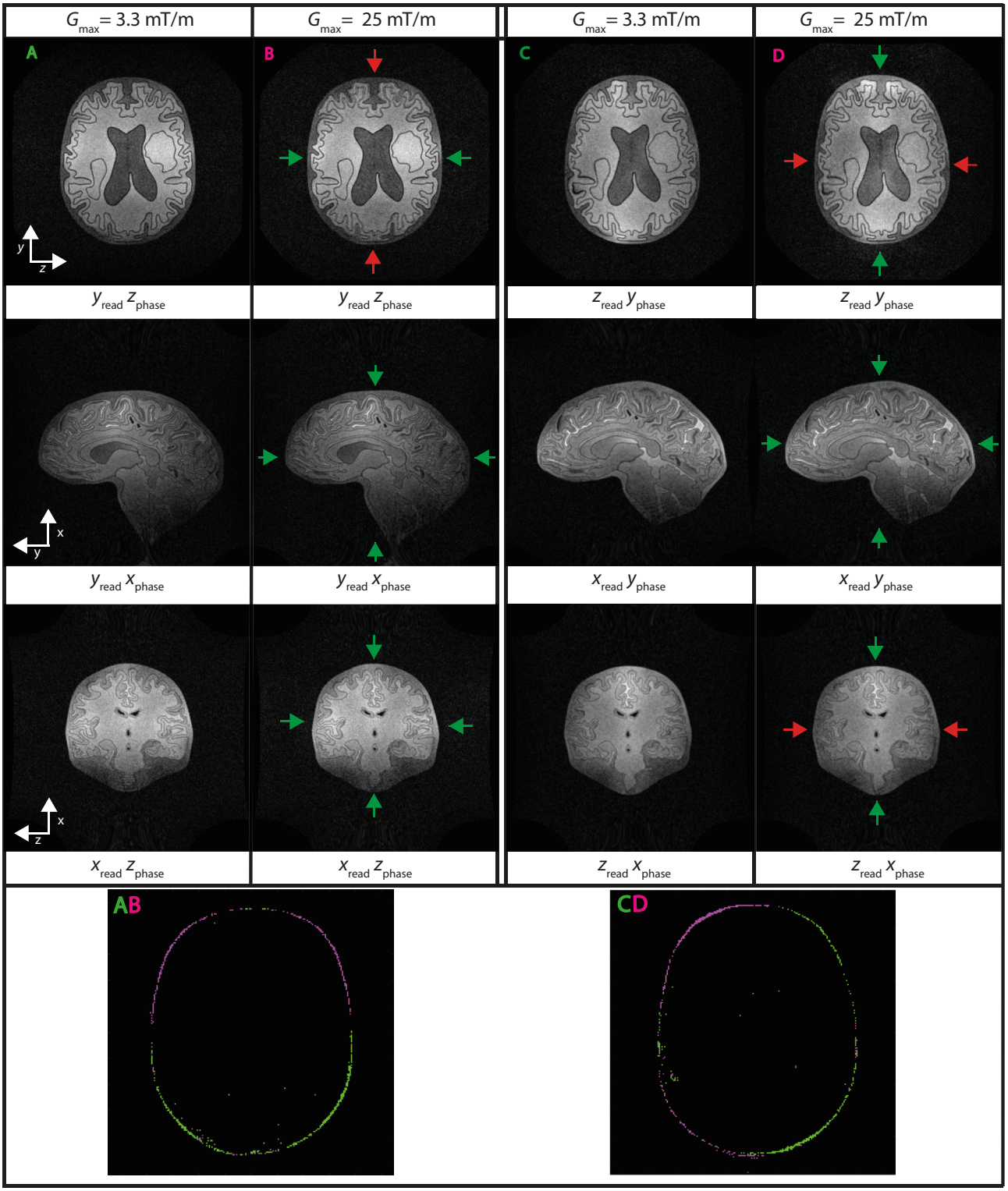

FIGURE 6 Phantom images obtained with the 2D SE sequence shown in 3(A,D), used to show the effects of the self-squared combined with the cross-term. Warping with respect to the reference image is visible in the top row. At the bottom of the figure the warped images are subtracted from the reference image to create a difference image. Here the green shows the reference and purple the warped image. Acq param: FOV: 280x280 mm, Data Matrix: 280x280, TR/TE = 900/65 ms, BW = 40 KHz, τ_d = 21 ms, NA = 6.

Figure 7 shows the results of the phase measurements on the stationary phantom. The left-hand side shows the result when simultaneously playing the y and z gradients, the cross-term creates a phase difference with a yz spatial dependency. Measurements of the other orientations show no phase error confirming the single cross-term. The

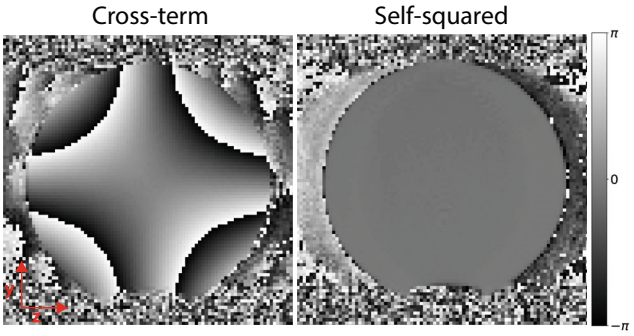

FIGURE 7 Phase measurements of a stationary phantom using anti-symmetric bipolar pulses of 5 ms with a gradient strength of 5 mT/m. The left figure shows the phase introduced by concomitant field cross-term when playing the bipolar pulse simultaneously with the readout dephasing. In the right figure the same sequence is used but with the gradient lobes applied sequentially.

same measurements but without overlap of the gradient lobes result in no phase difference within the phantom. The figure shows that the phase error is not sufficient to create visible spatial warping in the image, but does result in multiple phase wraps.

5 | DISCUSSION AND CONCLUSIONS

Concomitant fields and their effects on images are significantly different for Halbach-based systems when compared to conventional MRI systems. Distortions appear mainly in the outer parts of the transverse plane, as opposed to at the extremities in the head-foot direction. Another major difference is the single cross-term which is only evident when simultaneously using transverse gradients. This term causes warping if a dephasing frequency gradient is applied simultaneously with the phase encoding gradient. Simultaneously applying two-phase encoding gradients for 3D imaging was not discussed in this work, however simulations reveal additional blurring with spatial dependency yz. The cross-term is gradient polarity dependent, and therefore the warping can also appear mirrored to that demonstrated here in the phantom study.

To investigate when the concomitant modes $\ell = +1$ and $\ell = 0$ play a role the absolute value of the coupling term ($\mathbf{q}_{-1}^{H}\mathbf{p}_{\ell}$) can be displayed as a function of ϵ. It turns out that the other modes become significant only for $\epsilon > 0.2$ (for a 46 mT system and a 250 mm FOV, 37 mT/m gradients would be required). This is beyond the capabilities of the system used in this work and it suffices to consider the simplified model of Equation (17). In the Figure S2 the behavior of these modes can be found.

The expected maximum displacement of a pixel caused by the cross-term as created with the sequences shown in Figure 3B,D, and calculated using Equation (21), is displayed as a function of ϵ for a 250 mm Diameter Spherical Volume (DSV) in Figure 8. The red curve corresponds to the Halbach-based MRI cross-term, which leads to double the displacement of a conventional MRI cross-term shown with the blue curve. Typical MRI systems, and their expected maximum warping are indicated in the figure. For the Halbach system a maximum displacement of 2.5 mm is expected. However, this effect appears at the edges of a 250 mm DSV. The tube phantom images in Figure 4 shows that the warping is very subtle using the pulse sequences demonstrated here.

In previous work it was deemed sufficient to only use the $\frac{1}{2B_0}$ terms of the Taylor series to approximate $|\mathbf{B}|$. However, this only holds for small values of ϵ. In Figure 9 the

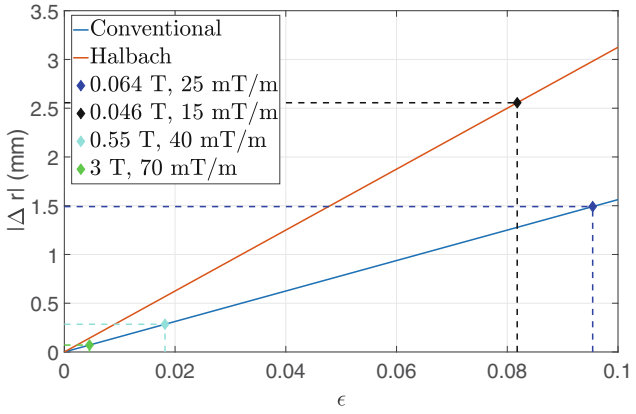

FIGURE 8 Maximum displacement created by cross-term warping within a 250 mm DSV as a function of ϵ. The red curve indicates warping corresponding to a Halbach-based systems while the blue curve corresponds to conventional systems. In the figure different systems and their corresponding maximum warping are indicated.

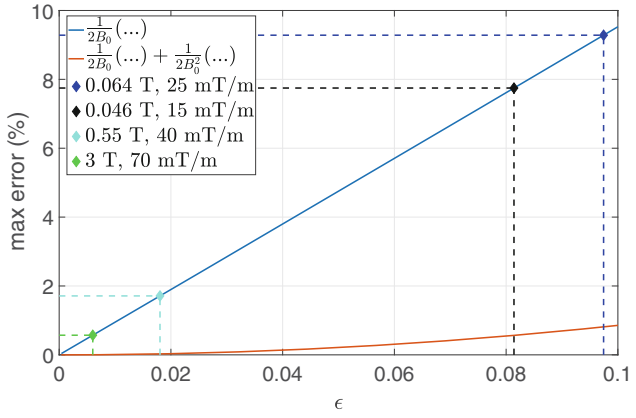

FIGURE 9 Maximum error made using the Taylor expansion to approximate $|\mathbf{B}|$ against values of ϵ, different systems are indicated in the figure. Blue shows the error when only considering the $\frac{1}{2B_0}$ terms, red when also considering the $\frac{1}{2B_0^2}$ terms.

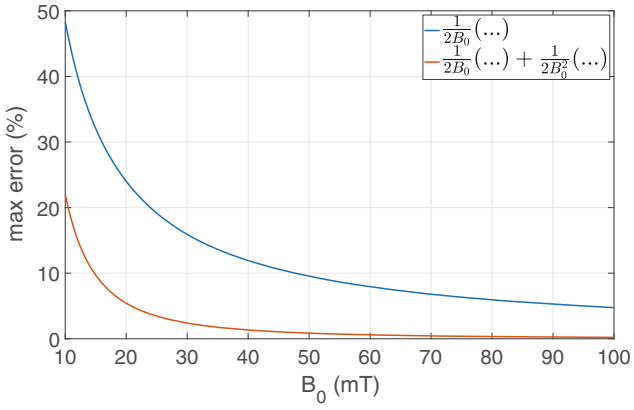

FIGURE 10 Maximum error made using the Taylor expansion to approximate $|\mathbf{B}|$ against values of B_0. A 250 mm field of view and constant gradient of 20 mT/m are considered. Blue shows the error when only considering the $\frac{1}{2B_0}$ terms, red when also considering the $\frac{1}{2B_0^2}$ terms.

maximum error with respect to the ground truth is displayed for different values of ϵ. As an example a range of MRI systems are indicated in the figure. Systems operating at an $\epsilon > 0.05$ should consider taking into account higher orders or the exact expression when using correction methods. In Figure 10 these curves are reproduced for field strengths in the range 10–100 mT, using a 250 mm FOV and a typical maximum gradient strength of 20 mT/m.

An additional bipolar pulse was used to simulate the concomitant field effects corresponding to strong phase encoding and dephasing gradients. It can however also be used to mitigate concomitant field effects by placing the bipolar pulse on the opposing side of a 180-degree RF-pulse and tuning it such that it cancels the unwanted phase.[20,23] However, this only works under the assumption that Equation (6) represents the concomitant fields, which does not hold for large ϵ as was demonstrated in Figure 9. This is also important to consider when applying postprocessing correction schemes such as References 10,12, and 16. At lower field strengths it becomes more important to use the exact description of $|\mathbf{B}|$ to correct for phase errors.

As discussed strong readout gradients are not considered here due to their corresponding signal-to-noise ratio penalty. If they are used, the $|\mathbf{B}(\mathrm{g}^{\mathrm{r}})|$ term shown as a multiplication of k-space in Equation (13) is expected to also create an undesired weighing of the signal intensity and should be considered.

The relevance of the modes $\ell = -1$ and $\ell = 0$ is shown to be insignificant for the range of POC low-field systems that are now being designed, making it sufficient to consider only the phase errors. However, for experimental micro-tesla MRI or diffusion weighted imaging using strong gradients these modes might well come into play. The model described here can be used identify the potential artifacts and phase errors and correct for them.

The results discussed here can be extrapolated to other sequences. The simplest translation would be toward a conventional gradient echo sequence, which will have very much the same effects as shown here. The only difference being the 180-degree pulse which can balance out or change the direction of the distortions of the artifacts due to the inversion of the phase. Sequences which are potentially more susceptible to concomitant field effects are accelerated sequence such as EPI[14,15] and fast spin echo,[20,23] but also sequences which use spiral trajectories.[17,18,23] These have been shown to display distortions at lower values of ϵ. With fast spin echo the effect is expected to be dependent on the chosen trajectory (in-out, out-in, etc.) as this will effect how the phase propagates through successive echoes. Partial signal cancelation can also occur due to the inversion of the phase after each 180-degree pulse. For EPI this is, however, not the case and the error will increase with each echo, creating significant distortions which need to be corrected. Low-field POC systems intrinsically have a much less homogeneous B_0 field compared to a full body system. This makes the use of EPI and spiral trajectories not (yet) feasible on these scanners. In the future advanced sequence development on low-field POC systems may require concomitant field corrections. This work gives the initial equations for a Halbach-array-based system and shows that in the current state minimal warping and blurring is to be expected when using basic sequences.

ACKNOWLEDGMENTS

This work was supported by ERC Advanced Grant, PASMAR, 101021218. The authors want to thank Chloé Najac for creating the contents used to fill the phantoms and Tom O'Reilly for his gradient unwarping algorithm.

ORCID

Bart de Vos https://orcid.org/0000-0003-2697-5597

REFERENCES

1. Wald LL, McDaniel PC, Witzel T, Stockmann JP, Cooley CZ. Low-cost and portable MRI. *J Magn Reson Imaging*. 2019;52:686-696.
2. Sarracanie M, Salameh N. Low-field MRI: how low can we go? A fresh view on an old debate. *Front Phys*. 2020;8. doi:10.3389/fphy.2020.00172
3. Nakagomi M, Kajiwara M, Matsuzaki J, et al. Development of a small car-mounted magnetic resonance imaging system for human elbows using a 0.2 T permanent magnet. *J Magn Reson*. 2019;304:1-6.
4. Liu Y, Leong ATL, Zhao Y, et al. A low-cost and shielding-free ultra-low-field brain MRI scanner. *Nat Commun*. 2021;12:7238.

5. Sheth KN, Mazurek MH, Yuen MM, et al. Assessment of brain injury using portable, low-field magnetic resonance imaging at the bedside of critically ill patients. *JAMA Neurol*. 2021;78:41-47.
6. Mazurek MH, Cahn BA, Yuen MW, et al. Portable, bedside, low-field magnetic resonance imaging for evaluation of intracerebral hemorrhage. *Nat Commun*. 2021;12:5119.
7. Chetcuti K, Chilingulo C, Goyal MS, et al. Implementation of a low-field portable MRI scanner in a resource-constrained environment: our experience in Malawi. *Am J Neuroradiol*. 2022;43:670-674.
8. Obungoloch J, Muhumuza I, Teeuwisse W, et al. On-site construction of a point-of-care low-field MRI system in Africa. *NMR Biomed*. 2023;36:e4917.
9. Bernstein MA, King FK, Xiaohong JZ. Concomitant-field correction gradients. *Handbook of MRI Pulse Sequences*. Wiley Blackwell; 2004:292-304.
10. Nieminen JO, Ilmoniemi RJ. Solving the problem of concomitant gradients in ultra-low-field MRI. *J Magn Reson*. 2010;207:213-219.
11. Yablonskiy DA, Sukstanskii AL, Ackerman JJ. Image artifacts in very low magnetic field MRI: the role of concomitant gradients. *J Magn Reson*. 2005;174:279-286.
12. Myers WR, Mößle M, Clarke J. Correction of concomitant gradient artifacts in experimental microtesla MRI. *J Magn Reson*. 2005;177:274-284.
13. Bernstein MA, Zhou XJ, Polzin JA, et al. Concomitant gradient terms in phase contrast MR: analysis and correction. *Magn Reson Med*. 1998;39:300-308.
14. Weisskoff RM, Cohen MS, Rzedzian RR. Nonaxial whole-body instant imaging. *Magn Reson Med*. 1993;29:796-803.
15. Zhou XJ, Du YP, Bernstein MA, Reynolds HG, Maier JK, Polzin JA. Concomitant magnetic-field induced artifacts in axial Echo planar imaging. *Magn Reson Med*. 1998;39:596-605.
16. Du YP, Zhou XJ, Bernstein MA. Correction of concomitant magnetic field-induced image artifacts in nonaxial echo-planar imaging. *Magn Reson Med*. 2002;48:509-515.
17. King KF, Ganin A, Zhou XJ, Bernstein MA. Concomitant gradient field effects in spiral scans. *Magn Reson Med*. 1999;41:103-112.
18. King KF. Spiral scanning with anisotropic field of view. *Magn Reson Med*. 2005;39:448-456.
19. Noll DC, Meyer CH, Pauly JM, Nishimura DG, Macovski A. A homogeneity correction method for magnetic resonance imaging with time-varying gradients. *IEEE Trans Med Imaging*. 1994;10:629-637.
20. Zhou XJ, Tan SG, Bernstein MA. Artifacts induced by concomitant magnetic field in fast spin-Echo imaging. *Magn Reson Med*. 1998;40:582-591.
21. Norris DG, Hutchison JMS. Concomitant magnetic field gradients and their effects on imaging at low magnetic field strengths. *Magn Reson Imaging*. 1990;8:33-37.
22. Volegov PL, Mosher JC, Espy MA, Kraus RH. On concomitant gradients in low-field MRI. *J Magn Reson*. 2005;175:103-113.
23. Wang Z, Ramasawmy R, Feng X, Campbell-Washburn AE, Mugler JP, Meyer CH. Concomitant magnetic-field compensation for 2D spiral-ring turbo spin-echo imaging at 0.55T and 1.5T. *Magn Reson Med*. 2023;90:552-568.
24. O'Reilly T, Teeuwisse WM, Webb AG. Three-dimensional MRI in a homogenous 27 cm diameter bore Halbach array magnet. *J Magn Reson*. 2019;24:307.
25. O'Reilly T, Teeuwisse WM, Gans D, Koolstra K, Webb AG. In vivo 3D brain and extremity MRI at 50 mT using a permanent magnet Halbach array. *Magn Reson Med*. 2021;85:495-505.
26. Vos B, Parsa J, Abdulrazaq Z, et al. Design, characterisation and performance of an improved portable and sustainable low-field MRI system. *Front Phys*. 2021;9. doi:10.3389/fphy.2021.701157
27. Cooley CZ, Haskell MW, Cauley SF, et al. Design of sparse Halbach magnet arrays for portable MRI using a genetic algorithm. *IEEE Transactions on Magnetics*. 2018;54:1-12. doi:10.1109/TMAG.2017.2751001
28. Cooley CZ, McDaniel PC, Stockmann JP. A portable scanner for magnetic resonance imaging of the brain. *Nature Biomedical Engineering*. 2021;5:229-239.
29. Vos B, Fuchs P, O'Reilly T, Webb AG, Remis RF. Gradient coil design and realization for a Halbach-based MRI system. *IEEE Trans Magn*. 2020;56:1-8. doi:10.1109/TMAG.2019.2958561
30. Brown RM, Cheng YN, Haacke EM, Thompson MR. Signal detection concepts. *Magnetic Resonance Imaging: Physical Principles and Sequence Design*. Wiley Blackwell; 2014.
31. O'Reilly T, Webb AG. In vivo T1 and T2 relaxation time maps of brain tissue, skeletal muscle, and lipid measured in healthy volunteers at 50 mT. *Magn Reson Med*. 2022;87:884-895.

SUPPORTING INFORMATION

Additional supporting information may be found in the online version of the article at the publisher's website.

Figure S1. The normalized PSF shown in Equation 19 evaluated at two positions representing the center and edge of the brain phantom, using the scan parameters described in Figure 5.

Figure S2. The absolute value of the coupling term displayed against values of epsilon. The blue curve shows the main mode which is dominant for small values of epsilon.

How to cite this article: de Vos B, Remis RF, Webb AG. Characterization of concomitant gradient fields and their effects on image distortions using a low-field point-of-care Halbach-based MRI system. *Magn Reson Med*. 2024;91:828-841. doi: 10.1002/mrm.29879

APPENDIX

We start with the Bloch equation

$$\frac{\mathrm{d}\mathbf{M}(t)}{\mathrm{d}t} + \gamma|\mathbf{B}|\hat{\mathbf{u}} \times \mathbf{M} = 0, \tag{A1}$$

where the magnetic flux density is written as $\mathbf{B} = |\mathbf{B}|\hat{\mathbf{u}}$, with $|\mathbf{B}|$ the magnitude of $\mathbf{B}$ and $\hat{\mathbf{u}} = \mathbf{B}/|\mathbf{B}|$ a unit vector.

Writing this equation out in components and storing the components of the magnetization vector in the 3-by-1 array $\mathsf{m} = [M_x, M_y, M_z]^T$, the Bloch equation can be written in matrix-vector form as

$$\frac{\mathrm{d}\mathsf{m}(t)}{\mathrm{d}t} + \gamma|\mathbf{B}|\mathsf{U}\mathsf{m} = 0, \tag{A2}$$

where

$$\mathsf{U} = \begin{bmatrix} 0 & -u_z & u_y \\ u_z & 0 & -u_x \\ -u_y & u_x & 0 \end{bmatrix} \tag{A3}$$

and $u_i = B_i/|\mathbf{B}|$, $i = x, y, z$. With $\mathsf{m}_0 = [M_x^0, M_y^0, M_z^0]^T$ the 3-by-1 array containing the components of the magnetization at $t = 0$, the solution of the Bloch equation for $t > 0$ can be written in terms of a matrix-exponent as

$$\mathsf{m}(t) = e^{-\gamma|\mathbf{B}|\mathsf{U}t}\mathsf{m}_0. \tag{A4}$$

Note that since relaxation effects are ignored, the matrix-exponent is a rotation matrix and, consequently, $\|\mathsf{m}(t)\|_2 = \|\mathsf{m}_0\|_2$ for $t > 0$, that is, the magnitude of the magnetisation is constant and equal to the magnitude of the initial magnetization.

Determining the eigendecomposition of matrix U, we have $\mathsf{U}\mathsf{X} = \mathsf{X}\Lambda$, with $\Lambda = \mathrm{diag}(-\mathrm{j}, 0, \mathrm{j})$ a diagonal matrix with the eigenvalues of U on its diagonal and X a unitary matrix ($\mathsf{X}^H\mathsf{X} = \mathsf{X}\mathsf{X}^H = \mathsf{I}$) with the eigenvectors of U as its columns. Explicitly, this can be written as $\mathsf{X} = (\mathsf{x}_{-1}, \mathsf{x}_0, \mathsf{x}_{+1})$, with eigenvectors given by

$$\mathsf{x}_{-1} = n\begin{pmatrix} u_x u_y + j u_z \\ -(u_x^2 + u_z^2) \\ u_y u_z - j u_x \end{pmatrix}, \quad \mathsf{x}_0 = \begin{pmatrix} u_x \\ u_y \\ u_z \end{pmatrix}, \tag{A5}$$

and $\mathsf{x}_{+1} = \mathsf{x}_{-1}^*$, where $n = 1/\sqrt{2(u_x^2 + u_z^2)}$ and the asterisk denotes complex conjugation.

Having the eigendecomposition of matrix U available, the solution of the Bloch equation can be written as

$$\mathsf{m}(t) = \mathsf{X}e^{-\mathrm{j}\gamma|\mathbf{B}|\mathsf{S}t}\mathsf{X}^H\mathsf{m}_0, \tag{A6}$$

where the diagonal eigenvalue matrix is written as $\Lambda = \mathrm{j}\mathsf{S}$, with $\mathsf{S} = \mathrm{diag}(-1, 0, 1)$. Finally, since the initial magnetization is proportional to the spin density ρ,[30] we write $\mathsf{m}_0 = \rho(\mathsf{r}')\tilde{\mathsf{m}}_0$ and obtain

$$\mathsf{m}(t) = \rho(\mathsf{r}')\mathsf{X}e^{-\mathrm{j}\gamma|\mathbf{B}|\mathsf{S}t}\mathsf{X}^H\tilde{\mathsf{m}}_0. \tag{A7}$$